

On-Chip MXene Microsupercapacitors for AC-Line Filtering Applications

Qiu Jiang, Narendra Kurra, Kathleen Maleski, Yongjiu Lei, Hanfeng Liang, Yizhou Zhang, Yury Gogotsi,* and Husam N. Alshareef*

Microsupercapacitors (MSCs) with high energy densities offer viable miniaturized alternatives to bulky electrolytic capacitors if the former can respond at the kilo Hertz (kHz) or higher frequencies. Moreover, MSCs fabricated on a chip can be integrated into thin-film electronics in a compatible manner, serving the function of ripple filtering units or harvesters of energy from high-frequency sources. In this work, wafer-scale fabrication is demonstrated of MXene microsupercapacitors with controlled flake sizes and engineered device designs to achieve excellent frequency filtering performance. Specifically, the devices (100 nm thick electrodes and 10 μm interspace) deliver high volumetric capacitance (30 F cm^{-3} at 120 Hz), high rate capability (300 V s^{-1}), and a very short relaxation time constant ($\tau_0 = 0.45$ ms), surpassing conventional electrolytic capacitors ($\tau_0 = 0.8$ ms). As a result, the devices are capable of filtering 120 Hz ripples produced by AC line power at a frequency of 60 Hz. This study opens new avenues for exploring miniaturized MXene MSCs as replacements for bulky electrolytic capacitors.

1. Introduction

Aluminum electrolytic capacitors (AECs) are widely used for delivering pulse power and filtering/smoothing 120 Hz alternating current (AC) signals, which are produced by rectifying AC-line power of 60 Hz (the line power frequency used in the United States). However, AECs are bulky with low volumetric energy density; thus it is essential to develop miniaturized energy storage units that can replace AECs for both pulse power and AC-line filtering applications.^[1–5] For instance, line-powered circuits require stable direct current (DC) voltage

for reliable operation, while emerging technologies, such as the internet of things (IoT), wireless sensor networks, biosensors, medical implants, and wearable electronics, require compatible micro-power modules that can harvest and store pulse power for the design of “autonomous on-chip technology”.^[6–8] However, AECs suffer from bulky size due to their low volumetric energy density.

Pioneering work by Miller in 2010 demonstrated efficient AC-line filtering using graphene-based electrochemical capacitors (ECs) in a stacked configuration, a result which established high energy density electrical double layer capacitors as promising devices for AC-line filters.^[1] The key parameters in the design of AC-line filters based on ECs include: i) Good ohmic contact of electrode materials with current collectors to reduce the interfacial


impedance between the two; ii) high external surface area with large sized pores (should not be microporous) to minimize electrolyte resistance; iii) good electronic/ionic conductivity of electrode materials, especially layered materials without interparticle resistance.

Microsupercapacitors (MSCs) are evolving on-chip energy storage devices that can offer compatible integration with thin film electronics with a much higher power density and cycle life over microbatteries.^[5,6,9–11] Interdigitated electrode architectures can potentially achieve more efficient ionic transport, which is a key advantage over the sandwich (parallel electrode) configuration,^[12] especially in the case of 2D materials with flakes stacked parallel to the current collector. The sandwich design hinders ionic transport due to the presence of separator and larger distance between electrodes and offers inferior performance compared to in-plane interdigital design. Upon shortening the ion transportation pathways, we expect that the planar microsupercapacitor configuration can achieve good frequency response and be suitable for AC-line filtering applications. Furthermore, on-chip microsupercapacitors can offer as much as 50% gain in volumetric capacity over the sandwich configuration.^[9]

MSCs fabricated using carbonaceous materials such as carbide-derived carbon (CDC),^[13] onion-like carbon (OLC),^[14] laser scribed graphene (LSG),^[15] and other materials^[16–19] have been demonstrated with high rate capabilities. Even though significant advances have taken place recently in terms of

Dr. Q. Jiang, Y. Lei, Dr. H. Liang, Dr. Y. Zhang, Prof. H. N. Alshareef
Materials Science and Engineering
Physical Science and Engineering Division
King Abdullah University of Science and Technology (KAUST)
Thuwal 23955-6900, Saudi Arabia
E-mail: husam.alshareef@kaust.edu.sa

Dr. N. Kurra, K. Maleski, Prof. Y. Gogotsi
Department of Materials Science and Engineering
A.J. Drexel Nanomaterials Institute
Drexel University
Philadelphia, PA 19104, USA
E-mail: gogotsi@drexel.edu

 The ORCID identification number(s) for the author(s) of this article can be found under <https://doi.org/10.1002/aenm.201901061>.

DOI: 10.1002/aenm.201901061

fabrication and material processing, the operational speeds of most of MSCs have not reached the level required for AC-line filtering applications.^[20–25] Lin et al., developed 3D micro-supercapacitors based on graphene and carbon nanotube carpet for AC-line filtering applications,^[26] showing a volumetric capacitance of 2 F cm^{-3} and relaxation time constant of 0.83 ms. Their study demonstrated that high temperature growth of carbon materials with open structures is an effective strategy to fabricate supercapacitors suitable for AC-line filtering.

However, it has been challenging to develop AC-line filtering function using solution processable pseudocapacitive materials, which typically suffer from limited electronic conductivity and hence poor charge transfer rates, as compared to electrical double layer capacitors (EDLCs). This limitation is rooted in the assumption that the kinetics of redox processes are slower than double layer processes in ECs,^[27] but is in fact due to the low conductivity of oxides and polymers used in pseudocapacitors. The high electronic conductivity of electrode material is one of the key parameters for high charge transfer rates besides the ionic conductivity and interfacial impedance.

Recently, solution processable 2D transition metal carbides (MXenes) have shown great promise as high rate pseudocapacitive materials for energy storage applications.^[28] Such kind of performance is due to their unique combination of 2D morphology, creating ionic channels between the layers, metallic conductivity ($8000\text{--}10\,000 \text{ S cm}^{-1}$), and fast surface redox reactions.^[29–33] For instance, titanium carbide ($\text{Ti}_3\text{C}_2\text{T}_x$, T_x is = O, –OH, and –F) MXene showed a specific volumetric capacitance up to 1500 F cm^{-3} along with ultra-high rate capability in three-electrode configuration.^[31] Extreme rate performance was recently reported for MXene-PEDOT composites in a sandwich device configuration.^[34]

In this study, we demonstrate that by controlling the lateral flake size and device design of MXene MSCs with interdigitated electrodes, it is possible to achieve excellent frequency response matching that of the electrolytic capacitors. Furthermore, we have been able to scale our fabrication process to the wafer scale, which proves the viability of our approach. To test the feasibility of our device, we demonstrate efficient and reliable filtering of voltage ripples using our MXene microsupercapacitors.

2. Result and Discussion

The $\text{Ti}_3\text{C}_2\text{T}_x$ MXene was synthesized by following the minimally intensive layer delamination (MILD) method.^[35] This protocol offers not only selective etching of Al from Ti_3AlC_2 MAX phase but also subsequent delamination of multilayer MXene stacks via manual shaking (see the Experimental Section). The aqueous Li ions present in the synthesis reaction are spontaneously intercalated due to negative surface charges on MXenes, facilitating delamination via simple agitation. It was reported that the MILD method produces higher quality $\text{Ti}_3\text{C}_2\text{T}_x$ MXene flakes compared to other existing etching and delamination protocols.^[35] As synthesized $\text{Ti}_3\text{C}_2\text{T}_x$ colloidal dispersions exhibit a Tyndall scattering effect, which is a manifestation of the inherent colloidal stability resulting from negative surface charges (Figure S1, Supporting Information). The delaminated $\text{Ti}_3\text{C}_2\text{T}_x$ dispersions from this method have

an average flake size above $1 \mu\text{m}$ which can be reduced below $0.5 \mu\text{m}$ by probe sonication (Figure 1a,b). Figure 1c shows the resulting transmission electron microscopy (TEM) images and flake size distributions obtained by scanning electron microscope (SEM). The data shows that the flake size of $\text{Ti}_3\text{C}_2\text{T}_x$ after sonication ranges from 100 to 600 nm, with an average size of $\approx 300 \text{ nm}$ (referred to as $\text{Ti}_3\text{C}_2\text{T}_x\text{-}0.3 \mu\text{m}$). In comparison, the flake size of $\text{Ti}_3\text{C}_2\text{T}_x$ before sonication ranges from 1 to $4 \mu\text{m}$, with an average of $1.7 \mu\text{m}$ (referred to as $\text{Ti}_3\text{C}_2\text{T}_x\text{-}1.7 \mu\text{m}$) (Figure 1d).

The size distribution of $\text{Ti}_3\text{C}_2\text{T}_x$ flakes was also estimated using dynamic light scattering (DLS), which matches quite well with the SEM images (Figure 1e), similar to previous studies on $\text{Ti}_3\text{C}_2\text{T}_x$.^[36] The surface functional groups of MXene endow it with a hydrophilic surface, which enables solution processing of MXenes to obtain thin films by a variety of techniques including vacuum assisted filtration, spray, spin, and dip coating with no surfactants.^[37–40] Four-point probe conductivity measurements showed that restacked $\text{Ti}_3\text{C}_2\text{T}_x\text{-}0.3 \mu\text{m}$ films (spray-coated) exhibit an electrical conductivity up to 900 S cm^{-1} compared to 4500 S cm^{-1} for $\text{Ti}_3\text{C}_2\text{T}_x\text{-}1.7 \mu\text{m}$ films. The low electrical conductivity of $\text{Ti}_3\text{C}_2\text{T}_x\text{-}0.3 \mu\text{m}$ arises from the pronounced contact resistance between the small flakes (Figure 1f and Figure S2a, Supporting Information).

The X-ray diffraction (XRD) patterns of spray-coated $\text{Ti}_3\text{C}_2\text{T}_x$ films on glass showed (002) peaks centered at 6.9° , confirming the restacking of $\text{Ti}_3\text{C}_2\text{T}_x$ layers with similar interlayer spacing (Figure 1g). Compared with $\text{Ti}_3\text{C}_2\text{T}_x\text{-}0.3 \mu\text{m}$, $\text{Ti}_3\text{C}_2\text{T}_x\text{-}1.7 \mu\text{m}$ film showed sharp (00 l) peaks, probably due to greater stacking in the case of large flakes. Moreover, based on Scherrer equation, the broader full width at half maximum (FWHM) of $\text{Ti}_3\text{C}_2\text{T}_x\text{-}0.3 \mu\text{m}$ compared to $\text{Ti}_3\text{C}_2\text{T}_x\text{-}1.7 \mu\text{m}$ also indicates random stacking of smaller flakes along the c -axis.

As illustrated in Figure 2a, MXene microsupercapacitor devices were fabricated using a photolithographic lift-off process followed by spray-coating of MXene dispersions. To form the predefined photoresist patterns, a $4 \mu\text{m}$ thick photoresist was coated onto SiO_2/Si substrate and then was exposed to ultraviolet (UV) light through a photomask. After developing in a developer solution, the exposed regions of photoresist were dissolved, leaving behind the interdigitated photoresist pattern (step 3, Figure 2a). A thin layer of Au (100 nm)/Ti (10 nm) was sputtered over the substrate as the current collector followed by O_2 plasma treatment to make the gold surface hydrophilic to ensure that MXene flakes are attached firmly and uniformly (Figure S3, Supporting Information). A thin layer of $\text{Ti}_3\text{C}_2\text{T}_x$ film was then coated onto the entire surface by spraying the water dispersion (1 mg mL^{-1}) with instantaneous drying achieved by blowing hot air (50°C) onto the substrate. The $\text{Ti}_3\text{C}_2\text{T}_x$ and Au/Ti metal layer deposited onto the unexposed photoresist regions were removed through an acetone lift-off process (step 6, Figure 2a). Due to the strong adhesion between the metal surface and $\text{Ti}_3\text{C}_2\text{T}_x$ sheets, peeling of the active material was not observed even after bath sonication used for the lift-off process. The surface texture and cross-section SEM images of spray-coated $\text{Ti}_3\text{C}_2\text{T}_x$ thin films are shown in Figure 2b,c.

The frequency response of MXene microsupercapacitors was investigated by electrochemical impedance spectroscopy

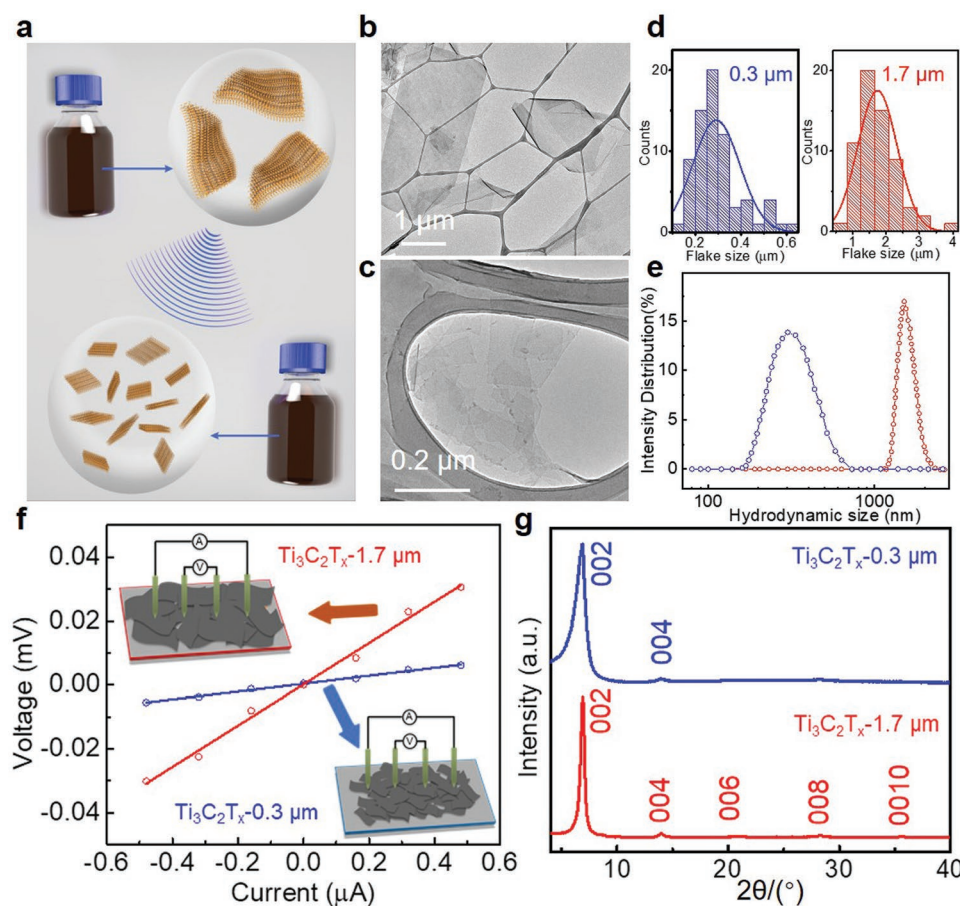
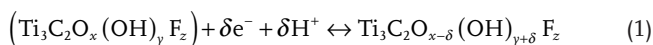


Figure 1. MXene colloids undergoing solution processing. a) Schematic showing flake size tuning by probe sonication. b,c) TEM images of $\text{Ti}_3\text{C}_2\text{T}_x$ with different flake sizes. d) Flake size distribution measured by scanning electron microscopy. e) Dynamic light scattering (DLS) intensity distribution of $\text{Ti}_3\text{C}_2\text{T}_x$ with different flake sizes. f) Current–voltage characteristics of spray-coated MXene films, inset shows the schematic of four-point probe conductivity measurement of thin films composed of different flake sizes. g) X-ray diffraction (XRD) patterns of $\text{Ti}_3\text{C}_2\text{T}_x$ films.

in polyvinyl alcohol/phosphoric acid (PVA/ H_3PO_4) gel electrolyte. The typical charge storage mechanism of $\text{Ti}_3\text{C}_2\text{T}_x$ in acid medium is explained as follows:^[41]



The impedance phase angles of the devices with the same width and interspacings of 100 μm (shown in the inset of Figure 2d) are plotted versus frequency and compared with a commercial aluminum electrolytic capacitor in Figure 2d. For AC-line filtering applications, the phase angle should be near -90° at 120 Hz.^[1] Previous density functional theory (DFT) calculations have shown that smaller $\text{Ti}_3\text{C}_2\text{T}_x$ flakes with more edge planes have stronger adsorption of N_2 , indicating that there is possibly a relationship between flake size and electrochemical reactivity.^[42] Not surprisingly, as can be seen in Figure 2d, our optimized $\text{Ti}_3\text{C}_2\text{T}_x$ -0.3 μm microsupercapacitor exhibits phase angles of -76° at 120 Hz, close to commercial AEC (phase angle of -84° at 120 Hz). In contrast, the $\text{Ti}_3\text{C}_2\text{T}_x$ -1.7 μm microsupercapacitor exhibited a phase angle of -60° at 120 Hz. The cross-over frequency at which the impedance phase angle reaches -45° is also an important parameter to study. The typical

cross-over frequencies (f) of $\text{Ti}_3\text{C}_2\text{T}_x$ -1.7 μm and $\text{Ti}_3\text{C}_2\text{T}_x$ -0.3 μm MSCs are found to be 220 and 1100 Hz, respectively.

Amazingly, although $\text{Ti}_3\text{C}_2\text{T}_x$ -0.3 μm has lower electrical conductivity compared to $\text{Ti}_3\text{C}_2\text{T}_x$ -1.7 μm , its equivalent series resistance (ESR) value is slightly lower (ESR, 0.2 $\Omega\text{ cm}^2$) than that of $\text{Ti}_3\text{C}_2\text{T}_x$ -1.7 μm (ESR, 0.5 $\Omega\text{ cm}^2$) (Figure 2e). This indicates that ion transport and accessibility are equally important besides the electronic conductivity of the films. In this case, a typical electronic conductivity of a few hundred S cm^{-1} is enough for high rate charge/discharge provided that the films have sufficient ionic conductivity.^[1] There are no semicircles observed in the high frequency region for both cases, indicating that negligible interfacial impedance issues. We expect that the oxygen plasma treatment of Au surface results in strong adhesion of MXene flakes, giving rise to near ohmic contacts. Furthermore, our results show that the $\text{Ti}_3\text{C}_2\text{T}_x$ -0.3 μm film has a more capacitive nature toward lower frequencies compared to $\text{Ti}_3\text{C}_2\text{T}_x$ -1.7 μm , as a more vertical line is observed. This can be explained by the relatively shorter ion transport path and lesser face to face restacking of the sheets for $\text{Ti}_3\text{C}_2\text{T}_x$ -0.3 μm films compared to $\text{Ti}_3\text{C}_2\text{T}_x$ -1.7 μm , as shown in inset of Figure 2e.

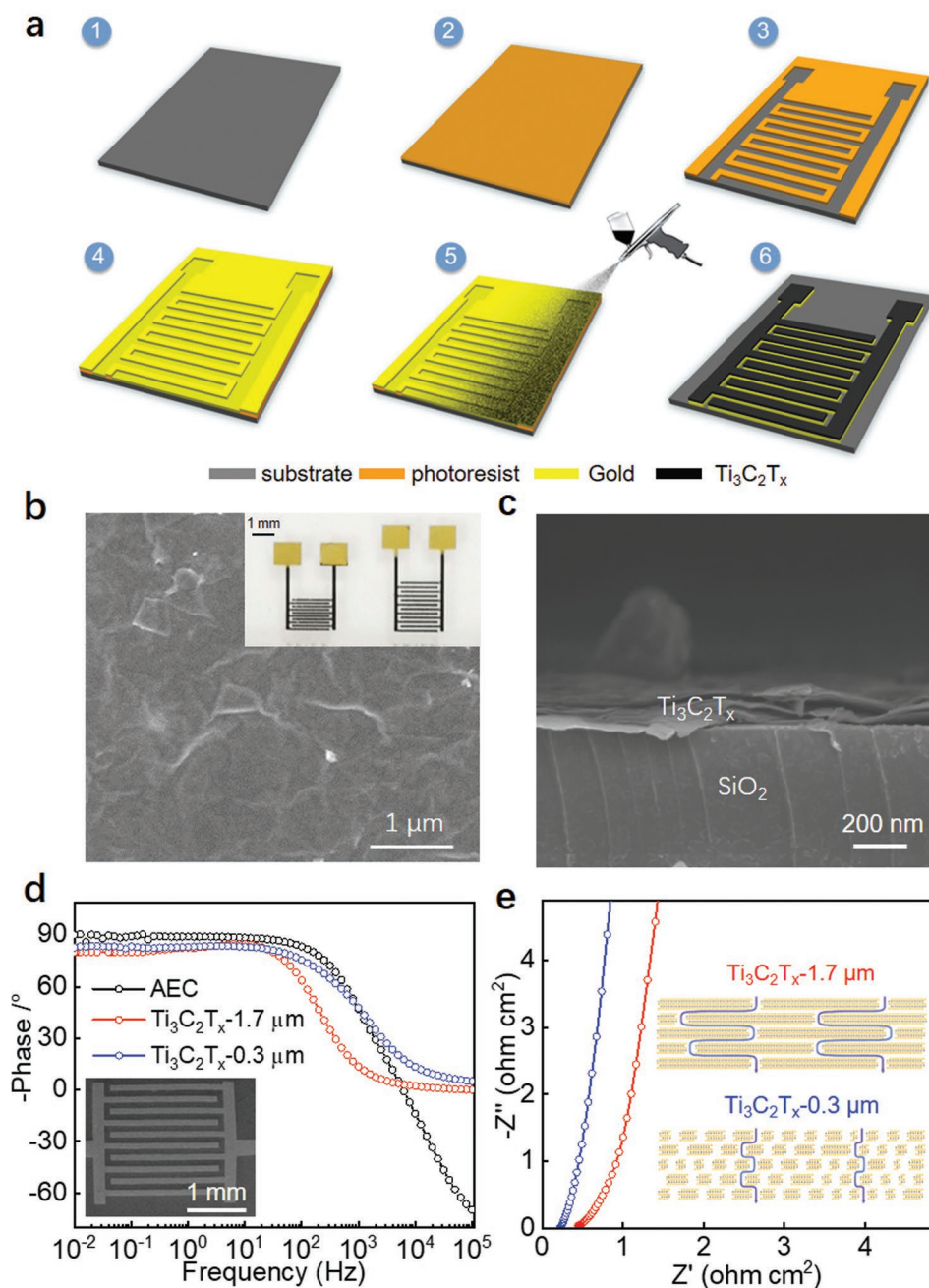


Figure 2. Fabrication of MXene microsupercapacitors a) Schematic illustration of the fabrication process of MXene microsupercapacitors including: photoresist coating (Panel 1–2), UV exposure through the photo mask followed by development (Panel 2–3), sputtering of Au/Ti (Panel 3–4), spray coating of $\text{Ti}_3\text{C}_2\text{T}_x$ (Panel 4–5), and final device after lift-off process in acetone (Panel 6). b) Planar and c) cross-sectional SEM images showing uniform coating of $\text{Ti}_3\text{C}_2\text{T}_x$ on gold, inset in (b) shows the digital photos of the MXene microsupercapacitor device. d) Bode phase angle plots of $\text{Ti}_3\text{C}_2\text{T}_x$ -0.3 and $\text{Ti}_3\text{C}_2\text{T}_x$ -1.7 μm microsupercapacitors, inset shows the optical photograph of MXene interdigitated fingers. e) Corresponding Nyquist spectra, inset shows schematic illustrations of the typical ion diffusion path ways for two types of thin films used in this study.

Cyclic voltammograms (CVs) of a $\text{Ti}_3\text{C}_2\text{T}_x$ -0.3 μm MSC exhibit rectangular behavior with high rate capability (Figure 3a). These CVs retain quasi-rectangular shapes even at a high scan rate of 300 V s^{-1} (Figure 3b). The ultra-high scan rate capability can be attributed to accessibility of the entire volume of the thin film to the electrolyte ions with little diffusion limitations. For an ideal capacitor, which has constant capacitance, the current response

should be linearly proportional to the scan rate based on the definition of capacitance ($C = I/\text{scan rate}$). The current response of our devices exhibits linear dependence on scan rates up to 300 V s^{-1} (Figure 3c), which is the highest rate among all reported MXene microsupercapacitors (Figure 3d).^[37,40,43] In contrast, CVs of the large-flake $\text{Ti}_3\text{C}_2\text{T}_x$ can retain a rectangular shape at a maximum scan rate of 30 V s^{-1} (the pure MXene

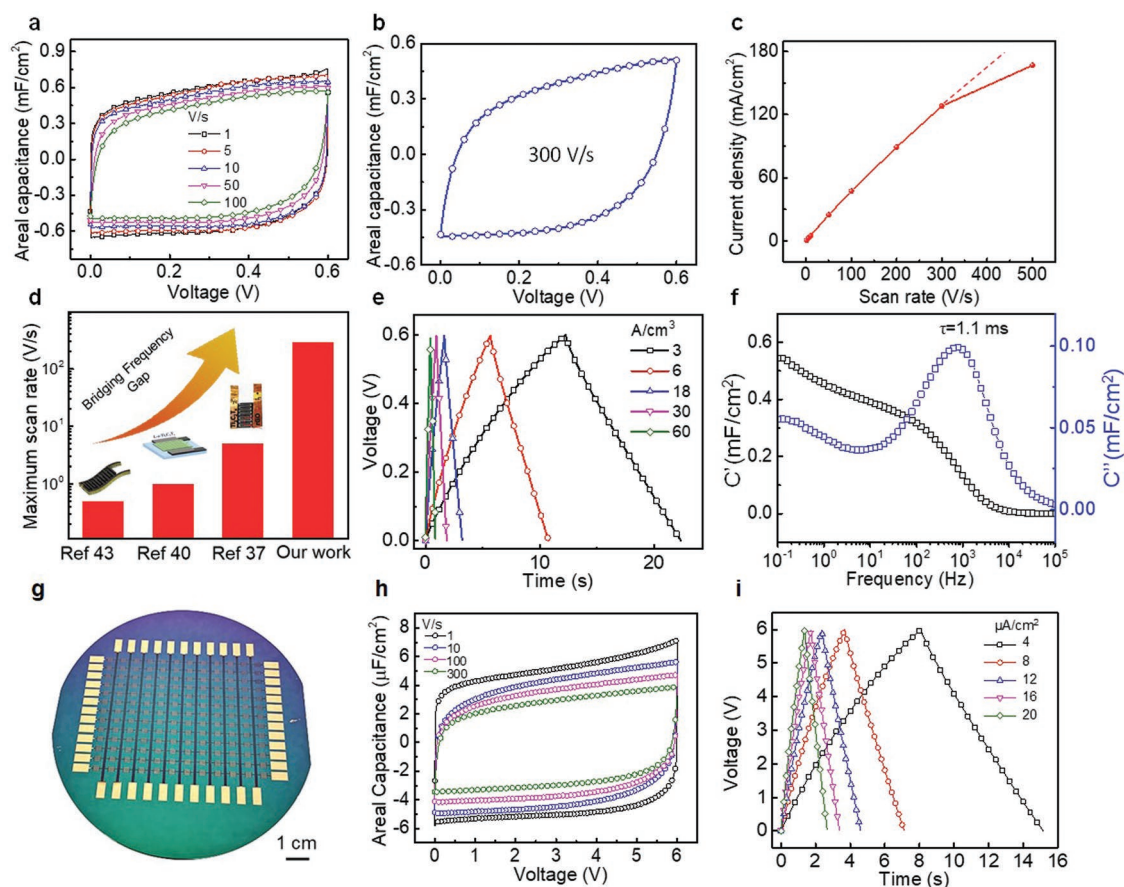


Figure 3. Electrochemical performance of $\text{Ti}_3\text{C}_2\text{T}_x$ -0.3 μm microsupercapacitors using PVA/ H_3PO_4 gel electrolyte. a,b) CV curves of $\text{Ti}_3\text{C}_2\text{T}_x$ -0.3 μm microsupercapacitor measured at different scan rates. c) Discharge current densities (values are taken at 0.3 V) as a function of scan rate. d) Rate performance comparing our devices with other MXene based microsupercapacitors. e) Galvanostatic charge-discharge profiles of $\text{Ti}_3\text{C}_2\text{T}_x$ -0.3 μm microsupercapacitor at different current densities. f) C' and C'' versus frequency for $\text{Ti}_3\text{C}_2\text{T}_x$ microsupercapacitor. g) Digital photograph showing the wafer scale fabrication of the MXene microsupercapacitors. h) CV curves of 10 microsupercapacitors connected in series at various scan rates i) and galvanostatic charge and discharge curves.

film without gold has a maximum scan rate of 3 V s^{-1} , Figure S4a, Supporting Information). Though $\text{Ti}_3\text{C}_2\text{T}_x$ thin films exhibit broad redox peaks in the three-electrode configuration (Figure S5, Supporting Information), the device showed quite rectangular CVs. This indicates that MXene electrodes exhibit typical capacitive behavior with superior electronic conductivity compared with other solution processable nanomaterials.^[44]

However, at a scan rate of 1 V s^{-1} , both $\text{Ti}_3\text{C}_2\text{T}_x$ -0.3 and $\text{Ti}_3\text{C}_2\text{T}_x$ -1.7 μm showed similar areal capacitance of about 0.5 mF cm^{-2} (Figure S4b, Supporting Information), suggesting that the flake size may not play a critical role in the maximum possible capacitance at low scan rates, since ions have enough time to access the entire volume of the film. The galvanostatic charge/discharge curves in Figure 3e show symmetric triangular-shaped curves. The Ohmic drop is small even at a high current density of 60 A cm^{-2} , which is a result of the good conductivity of $\text{Ti}_3\text{C}_2\text{T}_x$ electrodes. Figure 3f displays the real (C') and imaginary (C'') capacitances of the $\text{Ti}_3\text{C}_2\text{T}_x$ -0.3 μm microsupercapacitor, which were extracted from the EIS spectra. The characteristic relaxation time constant (τ_0) can be obtained from the frequency (f_0) at which imaginary capacitance C''

reaches the maximum value.^[45] It is the time required for discharging a capacitor with an energy efficiency greater than 50%. Capacitive behavior dominates at frequencies below τ_0 and resistive behavior at frequencies above τ_0 . The characteristic relaxation time constant ($\tau_0 = 1/f_0$) was estimated to be 1 ms, which is much better than the typical activated carbon EDLCs (usually a characteristic response time of $\approx 1 \text{ s}$).^[46] Capacitance at 120 Hz is estimated to be $\approx 300 \text{ μF cm}^{-2}$ from real capacitance C' , at an impedance of $2 \Omega \text{ cm}^2$, yielding a resistor-capacitor (RC) time constant (reflecting how fast the capacitor can be charged/discharged) of 0.6 ms. Such kind of RC time constant of capacitors is sufficient for 120 Hz filtering applications (8.3 ms). The corresponding volumetric capacitance is calculated to be 30 F cm^{-3} . For full-wave rectifier line filtering applications, the ripple (r) in the final output is approximated as

$$r = \frac{1}{2fRC} \quad (2)$$

where f is frequency and R is load resistance.^[47] The amount of capacitance is critical for a given level of ripples, while the

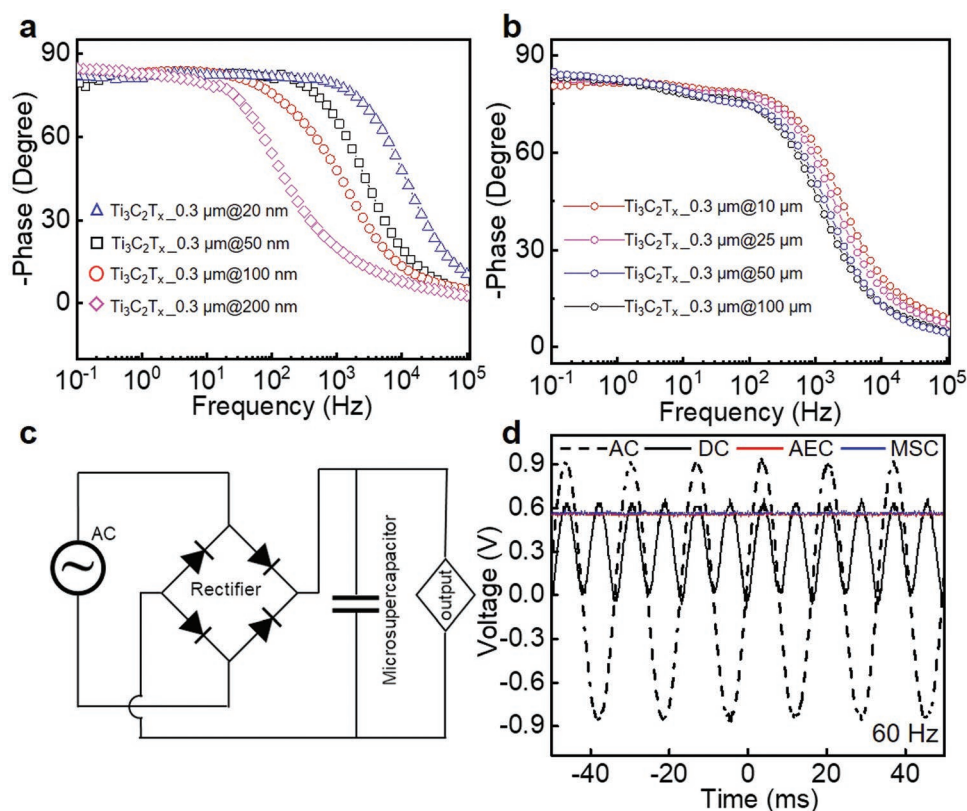


Figure 4. AC-line filtering performance of MXene microsupercapacitors. Comparison of phase angle versus frequency for $\text{Ti}_3\text{C}_2\text{T}_x$ -0.3 μm microsupercapacitors with different a) electrode material thickness and b) interfinger spacings. c) Schematic diagram of the AC-line filtering circuit. d) Output voltage signal after filtering using the MXene microsupercapacitor, comparing with the output voltage signal produced using commercial AEC.

voltage window of the capacitor restricts the maximum input voltage. Thus, large capacitances and high working voltages are two key parameters for optimizing performance, which can be given by the charge ($Q = C \cdot V$) of the device.^[1] The MXene microsupercapacitors stored a charge of 18 FV cm⁻³ (or C cm⁻³), compared to 0.14 FV cm⁻³ for a low-voltage Al-electrolytic capacitor (KDK, Tokyo, Japan), showing that MXene MSCs can have comparable rate capability while occupying a much smaller volume. Figure 3g shows 100 integrated MSCs fabricated on a 4 in. SiO_2/Si wafer, a great advancement compared to other reports, which lack compact integration and high voltage window operation for real applications. Wafer-scale fabrication of microsupercapacitors with single and series-connected microsupercapacitors is very important for device applications.^[11,48] The CVs of 10 cells connected in series show nearly rectangular shape up to a scan rate of 300 V s⁻¹ with 6 V voltage window (Figure 3h). The galvanostatic charge-discharge profiles exhibited symmetric triangular shapes, with little voltage drop, and with excellent coulombic efficiency (Figure 3i). Besides silicon substrates, we have also fabricated large scale MSCs on flexible polyethylene terephthalate (PET) substrate, which can be useful for wearable electronics and sensing applications (Figure S6, Supporting Information).

Besides flake size, the frequency response of MSCs can be controlled by the thickness of the electrodes and spacing of the

fingers. When thickness was increased from 100 to 200 nm, a decrease in frequency response measured at -45° was observed (Figure 4a). In contrast, when the thickness of the $\text{Ti}_3\text{C}_2\text{T}_x$ -0.3 μm decreased from 100 to 20 nm, the phase angle at 120 Hz improved from -76° to -82°, while the cross-over frequency at -45° increased from 1100 to 11 000 Hz. Such a high cross-over frequency at a phase angle of -5° is superior to the reported electrochemical capacitors^[49–58] with different geometry configurations, as shown in Table S1 (Supporting Information). This significantly improved electrochemical performance due to the decreased transport distance of the ions as confirmed by the Nyquist plot (Figure S7a, Supporting Information). However, areal capacitance decreased from 0.5 to 0.1 mF cm⁻² when the thickness decreased from 100 to 20 nm (Figure S7b, Supporting Information). The trade-off between areal capacitance and frequency response is due to the electrode mass loading and ion accessibility. To confirm the influence of the ion transport path length, we have further fabricated $\text{Ti}_3\text{C}_2\text{T}_x$ microsupercapacitors with the same finger width (100 μm) and thickness (100 nm) but different inter-finger spacings, as shown in Figure 4b. It is evident that devices with smaller interfinger spacings show faster response time, in agreement with previous studies.^[22] The cross-over frequencies of the devices (optical images for different electrode spacings of 100, 50, 25, and 10 μm are shown in Figure S8, Supporting Information) at -45° were found to be 1100, 1400, 1900, and 2600 Hz, respectively. When interfinger

spacing decreases, ions have shorter pathways to travel between the electrodes. As a result, the relaxation time constant of the device with 10 μm spacing decreases to 0.45 ms (Figure S9, Supporting Information). A summary of the performance of the MXene MSCs fabricated in this study is shown in Table S2 in the Supporting Information.

To demonstrate the AC-line filtering with MXene MSCs, a filter circuit was constructed as shown in Figure 4c. The 60 Hz sinusoidal AC input signal is first generated by a full-wave function generator with 50 Ω internal load resistance (filtering efficacy of a variety of capacitors fabricated in this study are under the same load) and then converted to a 120 Hz DC signal via a full-wave bridge rectifier (Figure S10, Supporting Information). After passing the rectified signal through the MXene microsupercapacitor, a substantially smoothed output signal is obtained (Figure 4d). As shown in Figure 4d, the AC signal with a peak voltage of 0.6 V was successfully converted and smoothed to a constant output positive voltage (≈ 0.56 V) using both our microsupercapacitor and a commercial 4 mF electrolytic capacitor. The successful conversion of the AC signal to constant voltage was enabled by the high volumetric capacitance and fast response of our $\text{Ti}_3\text{C}_2\text{T}_x$ microsupercapacitor. For comparison, we have also tested commercial AECs (with smaller capacitance than our device) and commercial activated carbon supercapacitors (phase angle of 0° at 120 Hz) and showed that MXene outperformed the commercial devices. Specifically, the former shows output voltage with spikes (Figure S11, Supporting Information) and the latter shows a 0 V output (Figure S12, Supporting Information). Furthermore, the AC-filtering function of the $\text{Ti}_3\text{C}_2\text{T}_x$ microsupercapacitor was demonstrated up to high frequencies of 600 and 1500 Hz (Figure S13, Supporting Information). In addition, cycling test of a single-cell microsupercapacitor showed almost no voltage drop even after 1 week of continuous operation (more than 7×10^7 cycles) using 60 Hz AC input sinusoidal signals (Figure S14, Supporting Information).

While this study indicates robust operation of MXene microsupercapacitors for AC-line filtering applications, it is important to note that we expect further improvement by selecting other MXenes from more than 30 available compositions and optimizing the device design, such as further decrease in flake size and spacing/geometry of finger electrodes.

3. Conclusion

In summary, we have developed electrochemical microsupercapacitors for AC-line filtering applications using solution processable 2D MXene (titanium carbide) nanosheets. Our results show that the frequency response of the MXene MSCs are highly dependent on flake size, thickness of the electrodes, and spacing between the electrode fingers. Specifically, devices with 100 nm thick electrodes and 10 μm spacing delivered a volumetric capacitance of 30 F cm^{-3} at 120 Hz, performed well at 300 V s^{-1} , and had a relaxation time constant of $\tau_0 = 0.45$ ms, outperforming electrolytic capacitors ($\tau_0 = 0.8$ ms). The optimized MXene microsupercapacitors were produced at the wafer scale and could filter out pulsed DC voltage ripples. Given the good performance characteristics and scalability, it

can be concluded that MXene microsupercapacitors represent a viable alternative to bulky electrolytic capacitors for filtering and other applications.

4. Experimental Section

Synthesis of Delaminated $\text{Ti}_3\text{C}_2\text{T}_x$ MXene with Different Flake Sizes: All chemicals were used as received without further purification. Ternary carbide, Ti_3AlC_2 (MAX phase) powder was commercially procured from Carbon-Ukraine Ltd, particle size $< 40 \mu\text{m}$. $\text{Ti}_3\text{C}_2\text{T}_x$ MXene was synthesized via minimally intensive layer delamination method, in which selective extraction of aluminum from Ti_3AlC_2 was done through in situ HF-forming etchant as previously reported.^[35] The etching solution was prepared by adding 1 g lithium fluoride (LiF, Alfa Aesar, 98+%) to 20 mL of 9 M hydrochloric acid (HCl, Fisher, technical grade, 35–38%), followed by stirring for 5 min. 1 g of Ti_3AlC_2 powder was slowly added to the MILD etchant at 35°C and stirred for 24 h. The acidic suspension was washed with deionized (DI) water until $\text{pH} \geq 6$ via centrifugation at 3500 rpm (5 min per cycle) and decanting the supernatant after each cycle. Around $\text{pH} \geq 6$, stable dark green supernatant of $\text{Ti}_3\text{C}_2\text{T}_x$ was observed and then collected after 5 min of centrifugation at 3500 rpm. As prepared $\text{Ti}_3\text{C}_2\text{T}_x$ suspension has an average flake size above 1 μm . To obtain $\text{Ti}_3\text{C}_2\text{T}_x$ with smaller flake sizes, $\text{Ti}_3\text{C}_2\text{T}_x$ suspension was sonicated for 45 min by using a tip sonicator (Sonics, vibracell) with a 5 s ON pulse and a 5 s “OFF” pulse at an amplitude of 40% under stirring in an ice bath. After sonication, no sediment is observed and then the suspension was centrifuged at 3500 rpm for 10 min. The concentration of $\text{Ti}_3\text{C}_2\text{T}_x$ solution was measured by filtering specific amounts of colloidal solution through a polypropylene filter (3501 Coated PP, Celgard LLC, Charlotte, NC), followed by drying under vacuum at 70°C overnight.

Preparation of MXene Microelectrodes: SiO_2/Si substrates (Fisher Scientific) were cleaned by sequential bath sonication in acetone, isopropanol, and deionized water for 5 min each. Positive photoresist ECI AZ3027 was spun at 3000 rpm for 30 s to achieve $\approx 4 \mu\text{m}$ photoresist layer followed by soft baking at 100°C for 60 s. Photoresist layer was exposed through EVG contact aligner at a constant dose of 210 mJ cm^{-2} through the Cr/glass mask with the predesigned patterns. Interdigitated fingers have a typical width of 100 μm and length of 2000 μm , while varied interspacings of 25–100 μm . After exposure, samples were developed in AZ726 developer for 60 s, followed by rinsing immediately in deionized water. Samples were then dried and 100 nm Au/10 nm Ti was deposited by reactive ion sputtering (Equipment Support Co., Cambridge, England) with 400 W at 5 mTorr pressure.

Prior to spray-coating of MXene, gold-coated substrates were treated with O_2 plasma (Plasmaflo PDC-FMG, USA) for 2 min to make them hydrophilic. Before spray coating, $\text{Ti}_3\text{C}_2\text{T}_x$ suspensions with different flake sizes were centrifuged for 10 min at 3500 rpm. An airbrush (Anest iwata, Japan) containing MXene dispersion was used for spraying with instantaneous drying using a hot air gun. MXene suspensions with different flake sizes were directly sprayed onto the gold surface, followed by lift-off in acetone. During the mild bath sonication process (Figure S3, Supporting Information), no detachment of MXene from the substrate was observed. By controlling the amount of sprayed suspension, thickness of the MXene films can be varied.

Preparation of Gel Electrolyte: The polyvinyl alcohol (PVA)/ H_3PO_4 gel electrolyte was prepared as follows: 1 g of PVA powder (MW 89 000–98 000 g mol^{-1}) was added into 10 mL of deionized water and the mixture was heated to 85°C while stirring until the solution become clear. The solution was cooled to room temperature and then 0.8 g of phosphoric acid solution (85%) was added while stirring. The whole mixture was stirred for 24 h to get homogeneous solution at room temperature. After, the gel was kept in vacuum oven at room temperature for 2 h to remove bubbles from the solution. Before using the gel, the cross-linking was performed by mixing the as-prepared gel with glutaraldehyde (volume ratio of the gel to glutaraldehyde is 20:1). The mixture was used immediately before the complete curing stage.

Material Characterization: X-ray diffraction patterns were collected by a Bruker diffractometer (D8 Advance) with Cu K α radiation, $\lambda = 1.5406 \text{ \AA}$. The morphology and microstructure of the samples were characterized by a scanning electron microscope (Nova Nano 630, FEI).

I–V curve was measured by a four-probe electrical system (RZ2001i, Ozawa science). The lateral size distributions of the MXene sheets were obtained using dynamic light scattering (Zetasizer Nano ZS, Malvern Instruments). The concentration of the suspensions was maintained at 0.01 mg mL^{-1} , and the DLS average was taken over a total of four measurements for each sample, and all measurements were carried out at room temperature.

Electrochemical Measurements: The electrochemical measurements including cyclic voltammetry, galvanostatic charge-discharge (GCD), and electrochemical cycling stability were conducted at room temperature using a VMP3 electrochemical workstation (BioLogic, France). Electrochemical impedance spectroscopy (EIS) measurements were performed using a Modulab (Solartron Analytical) electrochemical workstation in the frequency range from 100 kHz to 0.01 Hz at an open circuit potential by applying a small sinusoidal potential signal with an amplitude of 10 mV.

Calculations: Areal specific capacitance C_A (mF cm^{-2}) of electrode materials was calculated from the CV curves by integrating the discharge portion using the following equation

$$C_A = \frac{1}{VA\nu} \int i dV \quad (3)$$

where i is the discharge current (mA), V is the potential window (V), ν is the scan rate (mV s^{-1}), and A is the area of the electrode (cm^2).

2-Electrode Configuration (Device Measurements): Areal capacitance (mF cm^{-2}) of the devices was calculated from the CV curves by integrating the discharge portion using the following equation

$$C = \frac{1}{VA\nu} \int i dV \quad (4)$$

where i is the discharge current (mA), V is the voltage window (V), ν is the scan rate (V s^{-1}), and A is the total area of fingers covered with the electrolyte. To calculate volumetric capacitance, areal capacitance was divided by thickness (cm) of the active materials.

Impedance Spectra: The real (C') and imaginary (C'') parts of capacitances were calculated using the following equations

$$C' = -Z'' / (2\pi f A |Z|^2) \quad (5)$$

$$C'' = Z' / (2\pi f A |Z|^2) \quad (6)$$

where $|Z|$ is the absolute value of impedance (Ω), Z' and Z'' are the real and imaginary components of impedance, f is the frequency (Hz), and A is the geometrical area of the devices.

RC time constants (τ_{RC}) at each frequency were calculated using the formula

$$\tau_{RC} = Z' C' \quad (7)$$

Supporting Information

Supporting Information is available from the Wiley Online Library or from the author.

Acknowledgements

Research reported in this publication was supported by King Abdullah University of Science and Technology (KAUST) under grant number OSR-CRG2016-2963. Authors thank Advanced Nanofabrication, Imaging

and Characterization Laboratory at KAUST for experimental support. Samantha Buczek is acknowledged for proof-reading of the manuscript.

Conflict of Interest

The authors declare no conflict of interest.

Keywords

ac-line filtering, high rate, microsupercapacitors, MXene

Received: March 30, 2019

Revised: May 3, 2019

Published online: May 28, 2019

- [1] J. R. Miller, R. A. Outlaw, B. C. Holloway, *Science* **2010**, 329, 1637.
- [2] J. R. Miller, *IEEE Electr. Insul. Mag.* **2010**, 26, 40.
- [3] D. P. Dubal, N. R. Chodankar, D. H. Kim, P. Gomez-Romero, *Chem. Soc. Rev.* **2018**, 47, 2065.
- [4] Z. L. Wang, *Nano Today* **2010**, 5, 512.
- [5] M. Beidaghi, Y. Gogotsi, *Energy Environ. Sci.* **2014**, 7, 867.
- [6] N. A. Kyeremateng, T. Brousse, D. Pech, *Nat. Nanotechnol.* **2017**, 12, 7.
- [7] Z. L. Wang, *Faraday Discuss.* **2014**, 176, 447.
- [8] Z. L. Wang, J. Chen, L. Lin, *Energy Environ. Sci.* **2015**, 8, 2250.
- [9] C. Lethien, J. Le Bideau, T. Brousse, *Energy Environ. Sci.* **2019**, 12, 96.
- [10] F. Wang, X. Wu, X. Yuan, Z. Liu, Y. Zhang, L. Fu, Y. Zhu, Q. Zhou, Y. Wu, W. Huang, *Chem. Soc. Rev.* **2017**, 46, 6816.
- [11] P. Zhang, F. Wang, M. Yu, X. Zhuang, X. Feng, *Chem. Soc. Rev.* **2018**, 47, 7426.
- [12] B. Mendoza-Sánchez, Y. Gogotsi, *Adv. Mater.* **2016**, 28, 6104.
- [13] P. Huang, C. Lethien, S. Pinaud, K. Brousse, R. Laloo, V. Turq, M. Respaud, A. Demortière, B. Daffos, P. L. Taberna, B. Chaudret, Y. Gogotsi, P. Simon, *Science* **2016**, 351, 691.
- [14] D. Pech, M. Brunet, H. Durou, P. Huang, V. Mochalin, Y. Gogotsi, P. L. Taberna, P. Simon, *Nat. Nanotechnol.* **2010**, 5, 651.
- [15] M. F. El-Kady, R. B. Kaner, *Nat. Commun.* **2013**, 4, 1475.
- [16] P. Zhang, J. Wang, W. Sheng, F. Wang, J. Zhang, F. Zhu, X. Zhuang, R. Jordan, O. G. Schmidt, X. Feng, *Energy Environ. Sci.* **2018**, 11, 1717.
- [17] P. Zhang, F. Zhu, F. Wang, J. Wang, R. Dong, X. Zhuang, O. G. Schmidt, X. Feng, *Adv. Mater.* **2017**, 29, 604491.
- [18] Y. He, P. Zhang, F. Wang, L. Wang, Y. Su, F. Zhang, X. Zhuang, X. Feng, *Nano Energy* **2019**, 60, 8.
- [19] J. Li, S. Sollami Delekta, P. Zhang, S. Yang, M. R. Lohe, X. Zhuang, X. Feng, M. Östling, *ACS Nano* **2017**, 11, 8249.
- [20] N. Kurra, Q. Jiang, A. Syed, C. Xia, H. N. Alshareef, *ACS Appl. Mater. Interfaces* **2016**, 8, 12748.
- [21] Y. Rangom, X. Tang, L. F. Nazar, *ACS Nano* **2015**, 9, 7248.
- [22] W. Liu, C. Lu, X. Wang, R. Y. Tay, B. K. Tay, *ACS Nano* **2015**, 9, 1528.
- [23] W.-W. Liu, Y.-Q. Feng, X.-B. Yan, J.-T. Chen, Q.-J. Xue, *Adv. Funct. Mater.* **2013**, 23, 4111.
- [24] V. Strauss, M. Anderson, C. L. Turner, R. B. Kaner, *Mater. Today Energy* **2019**, 11, 114.
- [25] Q. Zhou, M. Zhang, J. Chen, J. D. Hong, G. Shi, *ACS Appl. Mater. Interfaces* **2016**, 8, 20741.
- [26] J. Lin, C. Zhang, Z. Yan, Y. Zhu, Z. Peng, R. H. Hauge, D. Natelson, J. M. Tour, *Nano Lett.* **2013**, 13, 72.

- [27] B. E. Conway, *Electrochemical Capacitors: Scientific Fundamentals and Technological Applications*, Kluwer Academic/Plenum Publishers, New York **1999**.
- [28] B. Anasori, M. R. Lukatskaya, Y. Gogotsi, *Nat. Rev. Mater.* **2017**, *2*, 16098.
- [29] M. R. Lukatskaya, O. Mashtalir, C. E. Ren, Y. Dall'Agnese, P. Rozier, P. L. Taberna, M. Naguib, P. Simon, M. W. Barsoum, Y. Gogotsi, *Science* **2013**, *341*, 1502.
- [30] Y. Xia, T. S. Mathis, M. Q. Zhao, B. Anasori, A. Dang, Z. Zhou, H. Cho, Y. Gogotsi, S. Yang, *Nature* **2018**, *557*, 409.
- [31] M. R. Lukatskaya, S. Kota, Z. Lin, M. Q. Zhao, N. Shpigiel, M. D. Levi, J. Halim, P. L. Taberna, M. W. Barsoum, P. Simon, Y. Gogotsi, *Nat. Energy* **2017**, *2*, 17105.
- [32] N. Kurra, M. Alhabeb, K. Maleski, C. H. Wang, H. N. Alshareef, Y. Gogotsi, *ACS Energy Lett.* **2018**, *3*, 2094.
- [33] S. Yang, P. Zhang, F. Wang, A. G. Ricciardulli, M. R. Lohe, P. W. M. Blom, X. Feng, *Angew. Chem., Int. Ed.* **2018**, *57*, 15491.
- [34] G. S. Gund, J. H. Park, R. Harpalsinh, M. Kota, J. H. Shin, T. Kim, Y. Gogotsi, H. S. Park, *Joule* **2019**, *3*, 164.
- [35] M. Alhabeb, K. Maleski, B. Anasori, P. Lelyukh, L. Clark, S. Sin, Y. Gogotsi, *Chem. Mater.* **2017**, *29*, 7633.
- [36] K. Maleski, C. E. Ren, M. Q. Zhao, B. Anasori, Y. Gogotsi, *ACS Appl. Mater. Interfaces* **2018**, *10*, 24491.
- [37] C. Couly, M. Alhabeb, K. L. Van Aken, N. Kurra, L. Gomes, A. M. Navarro-Suárez, B. Anasori, H. N. Alshareef, Y. Gogotsi, *Adv. Electron. Mater.* **2018**, *4*, 1700339.
- [38] Q. Jiang, N. Kurra, M. Alhabeb, Y. Gogotsi, H. N. Alshareef, *Adv. Energy Mater.* **2018**, *8*, 1703043.
- [39] P. Salles, E. Quain, N. Kurra, A. Sarycheva, Y. Gogotsi, *Small* **2018**, *14*, 1802864.
- [40] Y. Y. Peng, B. Akuzum, N. Kurra, M. Q. Zhao, M. Alhabeb, B. Anasori, E. C. Kumbar, H. N. Alshareef, M. Der Ger, Y. Gogotsi, *Energy Environ. Sci.* **2016**, *9*, 2847.
- [41] M. R. Lukatskaya, S.-M. Bak, X. Yu, X.-Q. Yang, M. W. Barsoum, Y. Gogotsi, *Adv. Energy Mater.* **2015**, *5*, 1500589.
- [42] Y. Luo, G.-F. Chen, L. Ding, X. Chen, L.-X. Ding, H. Wang, *Joule* **2019**, *3*, 279.
- [43] N. Kurra, B. Ahmed, Y. Gogotsi, H. N. Alshareef, *Adv. Energy Mater.* **2016**, *6*, 1601372.
- [44] L. L. Zhang, X. S. Zhao, *Chem. Soc. Rev.* **2009**, *38*, 2520.
- [45] P. L. Taberna, P. Simon, J. F. Fauvarque, *J. Electrochem. Soc.* **2003**, *150*, A292.
- [46] J. R. Miller, A. F. Burke, J. R. Miller, A. F. Burke, A. F. Burke, *Electrochem. Soc.* **2008**, *17*, 53.
- [47] K. V. Cartwright, E. J. Kaminsky, *Phys. Educ.* **2017**, *11*, 1301.
- [48] K. U. Laszczyk, K. Kobashi, S. Sakurai, A. Sekiguchi, D. N. Futaba, T. Yamada, K. Hata, *Adv. Energy Mater.* **2015**, *5*, 1500741.
- [49] D. Pech, M. Brunet, P. L. Taberna, P. Simon, N. Fabre, F. Mesnilgrete, V. Conédéra, H. Durou, *J. Power Sources* **2010**, *195*, 1266.
- [50] C. Du, N. Pan, *J. Power Sources* **2006**, *160*, 1487.
- [51] K. Sheng, Y. Sun, C. Li, W. Yuan, G. Shi, *Sci. Rep.* **2012**, *2*, 247.
- [52] Y. J. Kang, Y. Yoo, W. Kim, *ACS Appl. Mater. Interfaces* **2016**, *8*, 13909.
- [53] J. Lim, U. N. Maiti, N. Y. Kim, R. Narayan, W. J. Lee, D. S. Choi, Y. Oh, J. M. Lee, G. Y. Lee, S. H. Kang, H. Kim, Y. H. Kim, S. O. Kim, *Nat. Commun.* **2016**, *7*, 10364.
- [54] T. Nathan-Walleiser, I. M. Lazar, M. Fabritius, F. J. Tölle, Q. Xia, B. Bruchmann, S. S. Venkataraman, M. G. Schwab, R. Mülhaupt, *Adv. Funct. Mater.* **2014**, *24*, 4706.
- [55] N. Kurra, M. K. Hota, H. N. Alshareef, *Nano Energy* **2015**, *13*, 500.
- [56] W. Gao, N. Singh, L. Song, Z. Liu, A. L. M. Reddy, L. Ci, R. Vajtai, Q. Zhang, B. Wei, P. M. Ajayan, *Nat. Nanotechnol.* **2011**, *6*, 496.
- [57] Z. S. Wu, Z. Liu, K. Parvez, X. Feng, K. Müllen, *Adv. Mater.* **2015**, *27*, 3669.
- [58] Y. Yoo, M.-S. Kim, J.-K. Kim, Y. S. Kim, W. Kim, *J. Mater. Chem. A* **2016**, *4*, 5062.